ARTICLE

# Nonradiative Plasmon Decay and Hot Carrier Dynamics: Effects of Phonons, Surfaces, and Geometry

Ana M. Brown,[†] Ravishankar Sundararaman,*,[‡] Prineha Narang,*,[†,‡] William A. Goddard III,[‡,§] and Harry A. Atwater*,[†,‡]

[†]Thomas J. Watson Laboratories of Applied Physics, [‡]Joint Center for Artificial Photosynthesis, and [§]Materials and Process Simulation Center, California Institute of Technology, 1200 East California Boulevard, Pasadena, California 91125, United States

ABSTRACT: The behavior of metals across a broad frequency range from microwave to ultraviolet frequencies is of interest in plasmonics, nanophotonics, and metamaterials. Depending on the frequency, losses of collective excitations in metals can be predominantly classical resistive effects or Landau damping. In this context, we present first-principles calculations that capture all of the significant microscopic mechanisms underlying surface plasmon decay and predict the initial excited carrier distributions so generated. Specifically, we include *ab initio* predictions of phonon-assisted optical excitations in metals, which are critical to bridging the frequency range between resistive losses at low frequencies and direct interband transitions at

high frequencies. In the commonly used plasmonic materials, gold, silver, copper, and aluminum, we find that resistive losses compete with phonon-assisted carrier generation below the interband threshold, but hot carrier generation *via* direct transitions dominates above threshold. Finally, we predict energy-dependent lifetimes and mean free paths of hot carriers, accounting for electron−electron and electron−phonon scattering, to provide insight toward transport of plasmonically generated carriers at the nanoscale.

KEYWORDS: surface plasmons, hot carriers, transport, resistivity, dielectric response, density functional theory
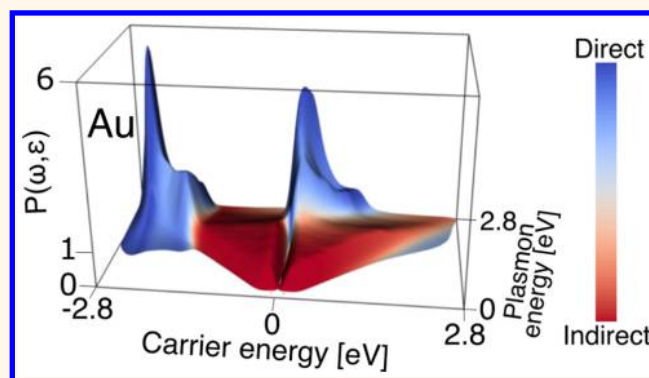
Plasmons provide a pathway to manipulate electromagnetic radiation at nanometer length scales[1,2] and femtosecond time scales.[3] Illumination of a metallic structure produces strong optical near-fields that initiate a cascade of processes with multiple outcomes, including the excitation of surface plasmons, their radiative decay to photons, and their nonradiative decay in the material.[4]

Nonradiative plasmon decay includes the generation of electron−hole pairs. These electron and hole energies depend on the material and the plasmon energy and are considered "hot" when significantly larger than those of thermal excitations at ambient temperatures. These hot carriers undergo fast internal relaxation but can be ejected into semiconductor and molecular systems, as clearly demonstrated in several recent device applications ranging from energy conversion and photocatalysis to photodetection. In particular, demonstrations of photochemistry driven by both hot electrons[5−8] and hot holes[9] raise interesting questions regarding the time scales of plasmonic hot carrier generation and transport.[10−12]

In addition to the visible and ultraviolet plasmonic response of metals, the behavior of metals at microwave and infrared frequencies is of broad interest.[13−15] Losses in metals can

proceed either through classical resistive dissipation or single-particle excitations. For plasmons, the collective excitations of electrons in metals, these excitations constitute Landau damping that results in generating highly energetic carriers. Direct optical excitation of carriers in most metals is allowed only above an interband threshold energy due to crystal momentum conservation. Below this threshold, which typically corresponds to optical frequencies, phonons provide the necessary momentum to circumvent this selection rule. Additionally, in metals, confinement of fields to the surface breaks translational invariance that can also provide the momentum necessary to excite intraband transitions.[16] These "surface-assisted" and phonon-assisted transitions are important contributors to losses in metals at infrared frequencies and, hence, important to understand from both fundamental and technological perspectives.[17]

First-principles calculations provide an opportunity to quantitatively analyze individually each microscopic mechanism underlying plasmon decay (Figure 1a) and gauge their relative
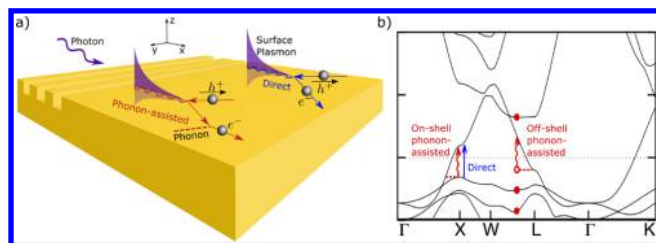

Figure 1. (a) Schematic for excitation and decay of surface plasmons. Surface plasmons excited, for example, through coupling to a grating or prism subsequently decay *via* direct and phonon-assisted transitions to generate hot electrons and holes. (b) Illustrations of direct, surface-assisted and phonon-assisted transitions on the band structure of gold. Surface-assisted transitions constitute the small but nonzero probability of nonvertical transitions due to the momentum distribution of the plasmon. The intermediate virtual state (empty circle) requires a sum over states (filled circles) in perturbation theory. When the intermediate state is a real state on the band structure (goes "on-shell"), it corresponds to a sequential process of electron–phonon scattering followed by a direct transition (or *vice versa*).

contributions in different materials and at different frequencies. These calculations examine the process at various time scales, separating effects due to the initial distribution of hot carriers and its subsequent transport. Such a detailed understanding, which is extremely challenging to extract from experiment, elucidates opportunities to enhance plasmonic hot carrier devices as well as their fundamental limits.

Previously, we studied in detail direct interband transitions in plasmonic metals[18] and showed that the plasmon-generated hot carrier distribution is extremely sensitive to details of the electronic band structure. Specifically, we found that in noble metals the positions of the d bands relative to the Fermi level result in much hotter holes than electrons; subsequent studies confirmed these results.[19] We also showed that the decay of surface plasmon polaritons is representative of decays in plasmonic nanostructures and that geometry effects on the generation of carriers are significant only at dimensions below 10 nm.

This article completes the theoretical picture of surface plasmon decay by adding *ab initio* calculations of phonon-assisted transitions and resistive losses. Previous first-principles calculations of phonon-assisted transitions treat indirect gap semiconductors only below their optical gap.[20,21] In extending such calculations to metals, we show that it is necessary to treat carefully the energy-conserving "on-shell" intermediate states that correspond to sequential processes (Figure 1b). We predict the contributions of these processes relative to direct transitions and compare the absolute decay rates to those estimated from experimentally measured complex dielectric functions for frequencies ranging from infrared to ultraviolet. Finally, we analyze the subsequent dynamics of the hot carriers generated, account for electron–electron and electron–phonon scattering, and present *ab initio* predictions for the strongly energy-dependent lifetimes and mean free paths of hot carriers.

RESULTS AND DISCUSSION

The decay of plasmons that determines generated carrier energy distributions and the subsequent scattering and transport of these carriers are both essential to the design of plasmonic hot carrier devices. Typically, scattering events thermalize the carriers and bring their energies closer to the Fermi level of the metal. Plasmonic hot carrier applications, on the other hand, require carriers far from the Fermi level to more efficiently drive both solid state and chemical processes. Various microscopic processes contribute to hot carrier generation as well as transport, and we quantitatively predict the contributions of the dominant processes for both aspects.

Within a quasiparticle picture, we include electron–electron and electron–lattice interactions in the quasiparticle energies as a part of the underlying electronic structure calculation. We also calculate electron–electron and electron–phonon scattering contributions to the quasiparticle line width, which determines carrier lifetimes and transport. The lowest-order process for the nonradiative decay of plasmons, which have negligible momentum compared to electrons in the material, is the direct generation of an electron–hole pair with net zero crystal momentum. This process is allowed above the interband threshold energy and dominates in that regime. Below the threshold energy, the electron–hole pair must have net momentum, and this momentum can be provided either by phonons in the bulk material or by surfaces in a nanostructure. We calculate all of these processes that have significant contributions and dominate in relevant energy ranges and length scales but ignore higher-order processes such as decays involving multiple electron–hole pairs or phonons, as these do not dominate in any regime.

In nanoscale systems, the electronic states are localized in space and are therefore no longer exact (crystal) momentum eigenstates by the uncertainty principle. This introduces a finite probability of direct plasmon decay into an electron–hole pair with net crystal momentum for plasmons below the interband threshold energy. For definiteness, we refer to these as geometry-assisted intraband transitions. Note, however, that the quasiparticle energies and line widths are not substantially altered at dimensions of ~10 nm and higher. In particular, confinement energies are $\hbar^2/(2m_e L^2) \sim 0.1$ eV only for dimensions $L \sim 0.6$ nm and line widths due to surface scattering are $\hbar v_F/(2L) \sim 0.1$ eV only for dimensions $L \sim 5$ nm (using the Fermi velocity $v_F \sim 1.5 \times 10^6$ m/s for noble metals), in contrast to the relevant plasmonic energy scales of ~1 eV. We therefore account for the geometry explicitly only to calculate geometry-assisted contributions to plasmon decay and use quasiparticle energies and line widths of the bulk material for all remaining contributions.

Plasmon Decay. In order to compare various contributions to surface plasmon decay with experiment on equal footing, we calculate contributions to the imaginary part of the dielectric tensor Im $\overline{\epsilon}(\omega)$ and relate the complex dielectric function to the plasmon decay rate. Specifically, the decay rate per unit volume, obtained by dividing the energy loss per unit volume[22] by the photon energy, is $\frac{1}{2\pi\hbar}\mathbf{E}^*(\mathbf{r})\cdot\mathrm{Im}\ \overline{\epsilon}(\omega)\cdot\mathbf{E}(\mathbf{r})$ at a point in the material where the electric field is $\mathbf{E}(\mathbf{r})$. For a surface plasmon polariton with wave vector $\mathbf{k}$ and angular frequency ω on the surface of a semi-infinite metal slab extending over $z < 0$, substituting the electric field profile of a single quantum[23,24] and integrating over space yields the total decay rate

$$\Gamma = \frac{\omega}{2L(\omega)|\gamma(z < 0)|}\lambda^* \cdot \mathrm{Im}\ \overline{\epsilon}(\omega) \cdot \lambda \tag{1}$$

Here, $L(\omega)$ is the quantization length for the plasmon determined by normalizing the energy density of the mode, $|\gamma(z < 0)|$ is the inverse decay length of the plasmon into the metal, and $\lambda \equiv \hat{k} - \hat{z}\, k/\gamma(z < 0)$ is the polarization vector. All of these quantities are fully determined by the experimental dielectric function and described in detail in refs 24 and 18.

We calculate the total "experimental" decay rate of plasmons as a function of frequency by using eq 1 directly with the complex dielectric functions measured by ellipsometry.[25]

Within the random phase approximation, direct interband transitions contribute[18]

$$\lambda^* \cdot \mathrm{Im}\ \overline{\epsilon}_{\mathrm{direct}}(\omega) \cdot \lambda$$
$$= \frac{4\pi^2 e^2}{m_e^2 \omega^2}\int_{\mathrm{BZ}}\frac{d\mathbf{q}}{(2\pi)^3}\sum_{n'n}(f_{\mathbf{q}n} - f_{\mathbf{q}n'})\delta(\varepsilon_{\mathbf{q}n'} - \varepsilon_{\mathbf{q}n} - \hbar\omega)$$
$$|\lambda \cdot \langle \mathbf{p}\rangle^{\mathbf{q}}_{n'n}|^2 \tag{2}$$

where $\varepsilon_{\mathbf{q}n}$ and $f_{\mathbf{q}n}$ are the energies and occupations of electronic quasiparticles with wave vectors $\mathbf{q}$ (in the Brillouin zone, BZ) and band index n, and $\langle \mathbf{p}\rangle^{\mathbf{q}}_{n'n}$ are momentum matrix elements. Note that the factor $(f_{\mathbf{q}n} - f_{\mathbf{q}n'})$ rather than $f_{\mathbf{q}n}(1 - f_{\mathbf{q}n'})$, as usually found in Fermi's golden rule, accounts for the difference between the forward and reverse processes. This is appropriate for the steady state change of plasmon number due to interactions with the electrons rather than the decay rate of a single plasmon mode. Hence, these two forms are each exact in different contexts and differ by the reverse process, which is the blackbody emission of plasmons due to room-temperature carriers. This process is completely negligible for $\hbar\omega \gg k_B T$ (≈ 0.026 eV), and hence we do not need to make this distinction when discussing plasmon decays in the near-infrared and optical frequency range. To account for finite carrier lifetimes, the energy-conserving δ function is replaced by a Lorentzian with half-width $\mathrm{Im}\Sigma_{\mathbf{q}n} + \mathrm{Im}\Sigma_{\mathbf{q}n'}$, where $\mathrm{Im}\Sigma_{\mathbf{q}n}$ is the total carrier line width due to electron–electron and electron–phonon scattering, as calculated using eq 7 and eq 8 below.

Substitution of eq 2 in eq 1 results exactly in the plasmon decay rate we previously derived using Fermi's golden rule within a fully quantum many-body formalism of the electrons and plasmons.[18] We calculate the energies and matrix elements with the same relativistic DFT+U method as ref 18, which produces band structures in excellent agreement with photoemission spectra. Since we use a spinorial electronic structure method to fully treat relativistic effects, the band indices include spin degrees of freedom.

Next, the contribution due to phonon-assisted transitions from second-order perturbation theory is[20,21]

$$\lambda^* \cdot \mathrm{Im}\ \overline{\epsilon}_{\mathrm{phonon}}(\omega) \cdot \lambda = \frac{4\pi^2 e^2}{m_e^2 \omega^2}\int_{\mathrm{BZ}}\frac{d\mathbf{q}'d\mathbf{q}}{(2\pi)^6}$$
$$\sum_{n'n\alpha\pm}(f_{\mathbf{q}n} - f_{\mathbf{q}'n'})\left(n_{\mathbf{q}'-\mathbf{q},\alpha} + \frac{1}{2} \mp \frac{1}{2}\right)$$
$$\delta(\varepsilon_{\mathbf{q}'n'} - \varepsilon_{\mathbf{q}n} - \hbar\omega \mp \hbar\omega_{\mathbf{q}'-\mathbf{q},\alpha}) \times$$
$$\left|\lambda \cdot \sum_{n_1}\left(\frac{g^{\mathbf{q}'-\mathbf{q},\alpha}_{\mathbf{q}'n',\mathbf{q}n_1}\langle\mathbf{p}\rangle^{\mathbf{q}}_{n_1 n}}{\varepsilon_{\mathbf{q}n_1} - \varepsilon_{\mathbf{q}n} - \hbar\omega + i\eta}\right.\right.$$
$$\left.\left.+ \frac{\langle\mathbf{p}\rangle^{\mathbf{q}'}_{n'n_1}g^{\mathbf{q}'-\mathbf{q},\alpha}_{\mathbf{q}'n_1,\mathbf{q}n}}{\varepsilon_{\mathbf{q}'n_1} - \varepsilon_{\mathbf{q}n} \mp \hbar\omega_{\mathbf{q}'-\mathbf{q},\alpha} + i\eta}\right)\right|^2 \tag{3}$$

where $\hbar\omega_{\mathbf{k}\alpha}$ is the energy of a phonon with wave vector $\mathbf{k}$ and polarization index α, $n_{\mathbf{k}\alpha}$ is the corresponding Bose occupation factor, and $g^{\mathbf{k}\alpha}_{\mathbf{q}'n',\mathbf{q}n}$ is the corresponding electron–phonon matrix element with electronic states labeled by wave vectors $\mathbf{q},\mathbf{q}'$ and band indices n,n' (with $\mathbf{k} = \mathbf{q}' - \mathbf{q}$ for crystal momentum conservation). The sum over $\pm$ accounts for phonon absorption as well as emission. Since the *ab initio* matrix elements couple all pairs of wave vectors in the Brillouin zone, they implicitly account for wrap-around (Umklapp) processes.

We calculate the phonon energies and electron–phonon matrix elements consistently using the same relativistic DFT+U approximation as for the electronic states. We use a Wannier representation to efficiently interpolate the phonon energies and matrix elements to calculate the Brillouin zone integrals in eq 3 accurately (see Methods section for details).

The imaginary part of the energy denominator, η, in the second line of eq 3 corresponds to the line width of the intermediate electronic state (with band index n_1). The value of η does not affect the phonon-assisted absorption at photon energies less than the optical gap of materials[20,21] and is usually treated as a numerical regularization parameter. However, above the optical gap (the interband threshold for metals), the real part of the denominator crosses zero, making the resulting singular contributions inversely proportional to η. These singular contributions correspond to sequential processes: electron–phonon scattering followed by a direct interband transition or *vice versa* (Figure 1). For a metal, including contributions from these sequential processes, this would lead to multiple counting of the direct transition. Scattering events preceding the optical transition are a part of the equilibrium Fermi distribution, while scattering events following the optical transition corresponds to the subsequent inelastic relaxation of the generated carriers. We eliminate this multiple counting by taking advantage of the η independence of the nonsingular part and the η^{-1} variation of the singular part and extrapolating from calculations done using two values of η (see Methods section for details).

In metals, the strong confinement of fields at the surface introduces an additional mechanism for intraband transitions. The exponential decay of the fields in the metal with inverse decay length $|\gamma(z < 0)|$ introduces a Lorentzian distribution in the momentum of the plasmon normal to the surface with width $\sim|\gamma(z < 0)|$. (This can also be interpreted in terms of the uncertainty principle.) This momentum distribution allows diagonal intraband transitions on the band structure (Figure 1b), which contribute a "surface-assisted" loss[16,26]

$$\mathrm{Im}\,\epsilon_{\mathrm{surface}}(\omega) = \frac{\omega_p^2}{\omega^3} \times \left(\frac{3}{4}|\gamma(z<0)|v_{\mathrm{F}}\right)\frac{2k^2}{k^2+|\gamma(z<0)|^2}$$

(4)

Here, $\omega_p = \sqrt{4\pi n e^2/m_e}$ is the bulk plasma frequency of the metal and $v_{\mathrm{F}} = (\hbar/m_e)\sqrt[3]{3\pi^2 n}$ its Fermi velocity, where n is the bulk carrier density of the metal. In nanoconfined geometries, such as spherical nanoparticles, the probability of intraband transitions due to crystal momentum nonconservation can be greatly enhanced, as shown by several numerical studies using free-electron jellium models.[27−29] We can calculate the decay rate of localized surface plasmons in a spherical nanoparticle using Fermi's golden rule with analytical free-electron eigenstates, dipole field profiles, and matrix elements and use eq 1 to express that rate as an effective Im ϵ contribution.

$$\mathrm{Im}\,\epsilon_{\mathrm{sphere}}(\omega) = \frac{\omega_p^2}{\omega^3} \times \frac{6v_F}{\pi^2 R}$$

(5)

where R is the radius of the spherical nanoparticle. This is similar to eq 4 except for dimensionless prefactors and the particle radius setting the length scale instead of the skin depth. See ref 26 for detailed derivations of these contributions.

The direct, surface/geometry-assisted, and phonon-assisted transitions considered above are the lowest-order processes for the decay of a plasmon to single-particle excitations, which correspond to the Landau damping of the plasmon on the Fermi sea.[30−32] Higher-order processes including multiple electron−hole pairs or multiple phonons are suppressed by phase-space factors at low energies and become important only at higher energies that are not usually accessed by surface plasmons.[3]

Apart from Landau damping, an additional source of plasmon loss is the intrinsic lifetime of the electronic states comprising the collective oscillation. This corresponds to a resistive loss in the material which we calculate using a linearized Boltzmann equation with a relaxation time approximation. We show in the Methods section that

$$\mathrm{Im}\,\epsilon_{\mathrm{resistive}}(\omega) = \frac{4\pi\sigma_0}{\omega(1+\omega^2\tau^2)}$$

(6)

where the zero-frequency conductivity σ_0 and the momentum relaxation time τ are derived from *ab initio* electronic states and electron−phonon matrix elements.

Figure 2 compares the plasmon line width and decay rates estimated directly from the experimentally measured complex dielectric functions with theoretical predictions for cumulative contributions from direct, surface-assisted, phonon-assisted transitions and resistive losses. For all the common plasmonic metals, aluminum and the noble metals, we find that direct transitions dominate above the interband threshold (∼1.6−1.8 eV for aluminum, gold, and copper and ∼3.5 eV for silver). The sum of all other contributions is less than 10% above threshold, and hence the cumulative results overlay the direct transition lines. In silver, the maximum plasmon frequency coincides with the interband threshold, and hence, there is no accessible frequency range for which direct transitions dominate. In aluminum, direct transitions are, in fact, possible at all frequencies due to a band crossing near the Fermi level,[18] but an additional channel for direct transitions with much higher density of states opens up at the effective threshold of ∼1.6 eV.
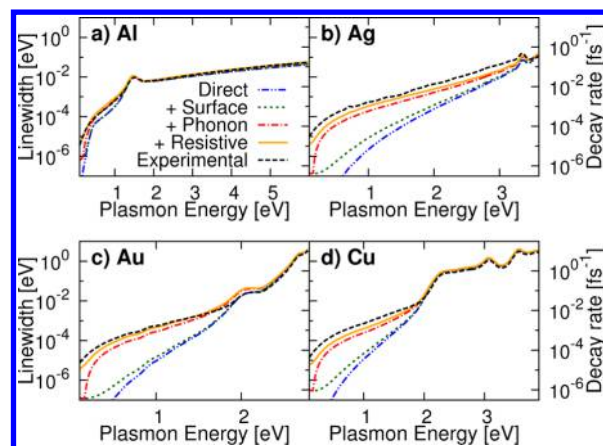

Figure 2. Comparison of calculated and experimental line widths (left axis) and decay rates (right axis) in (a) Al, (b) Ag, (c) Au, and (d) Cu. The theoretical curves indicate cumulative contributions from direct transitions alone ("Direct"), including surface-assisted transitions ("+Surface"), including phonon-assisted transitions ("+Phonon"), and including resistive losses ("+Resistive").

Below the threshold, direct transitions are forbidden (or for aluminum, are weak), and the contributions due to the other processes become important. For the ideal surface we consider here, surface-assisted processes contribute only a small fraction (at most 5%) of the experimental line width over the entire frequency range below threshold. Adsorption of molecules, localized surface states, and defects can induce additional surface-assisted contributions, which could be estimated in future work for specific cases using direct *ab initio* calculations of nanoscale geometries. Phonon-assisted transitions and resistive losses compete significantly and dominate the frequency range below the interband threshold. The relative importance of phonon-assisted transitions increases slightly with frequency, with resistive and surface-assisted losses dominating at very low frequencies (close to 0 eV in these plots), an approximately even split between the three processes at ∼1 eV, and a greater contribution from phonon-assisted transitions just below threshold.

The total line width predicted by a theory that includes all these contributions agrees very well with experiment over the entire range of frequencies.[25] Above threshold for the noble metals, the theoretical predictions overestimate experiment by ∼10−20%, which is the typical accuracy of optical matrix elements involving d electrons in density functional theory.[33] Below threshold, the total theory result underestimates the experimental value, but it is typically within a factor of 2. This may arise from material nonidealities that contribute additional losses and because our theoretical calculations estimate an ideal lower bound. In fact, the largest discrepancy is for silver because these ideal losses are the smallest, making nonidealities relatively more important. Also note that there is a significant spread in tabulated experimental dielectric functions for the noble metals,[25] with discrepancies a factor of 2 or higher in the imaginary parts at infrared frequencies. (We used the measurements that covered the greatest frequency range.) Therefore, more careful experimental measurements in that frequency range with higher-quality samples would be necessary and useful for a stricter comparison.

The results in Figure 2 are based on calculations at standard room temperature, $T = 298$ K. We expect the direct and surface-assisted contributions to be approximately independent

of temperature, the resistive contributions to decrease almost linearly with decreasing temperature, and the phonon-assisted contributions to reduce by a factor of 2 upon lowering the temperature (phonon emission persists while phonon absorption freezes out). Therefore, at very low temperatures, phonon-assisted transitions will dominate below threshold, while direct transitions continue to dominate above threshold.

Figure 3 compares the relative contributions due to all the above processes to absorption in the surface of bulk gold and
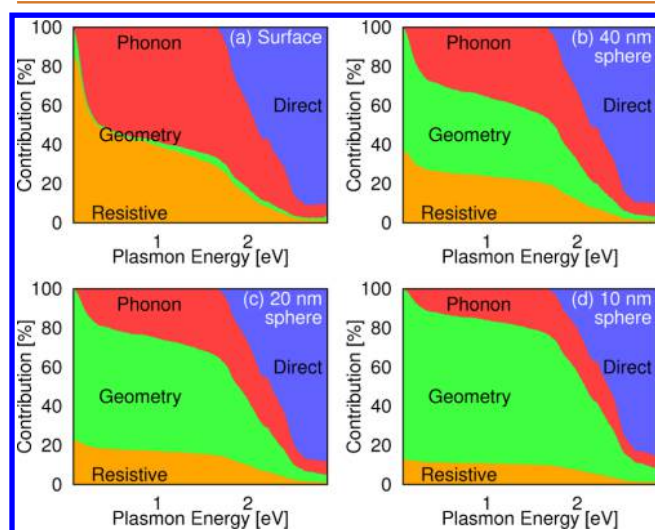

Figure 3. Comparison of resistive, geometry-assisted, phonon-assisted, and direct transition contributions to absorption in gold as a function of frequency for (a) semi-infinite surface or (b) 40 nm, (c) 20 nm, or (d) 10 nm diameter spheres. The surface/geometry contributions are negligible for the semi-infinite surface, aer comparable to the phonon-assisted and resistive contributions for a 40 nm sphere, and increase in inverse proportion with decreasing sphere diameter. Direct transitions dominate above threshold in all cases.

spherical gold nanoparticles of various sizes. Geometry-assisted intraband contributions are negligible for a semi-infinite surface and are comparable to the phonon-assisted and resistive contributions for a 40 nm diameter sphere below threshold. With decreasing particle size, the relative contributions of the geometry-assisted transitions increase in inverse proportion and dominate the subthreshold absorption for gold spheres smaller than 10 nm. However, direct transitions continue to dominate above the interband threshold even for these small spheres. Therefore, simplified treatment of localized plasmon decay in nanoparticles using jellium models that preclude direct transitions[27−29] is only reasonable for frequencies below the interband threshold. Those approximations are therefore reasonable for silver, where the interband threshold exceeds the dipole resonance frequency, but not for gold, copper, or aluminum.

Figure 4 shows the initial carrier distributions generated *via* direct and phonon-assisted transitions, which we calculate by histogramming the integrands in eq 2 and eq 3 by the initial (hole) and final (electron) state energies. The carrier distributions are plotted as a function of carrier energy (horizontal axis) and plasmon/photon energy (axis normal to the page). The color scale indicates the fraction of carriers generated by direct or phonon-assisted transitions. Note that carrier energies may exceed the plasmon energy with low
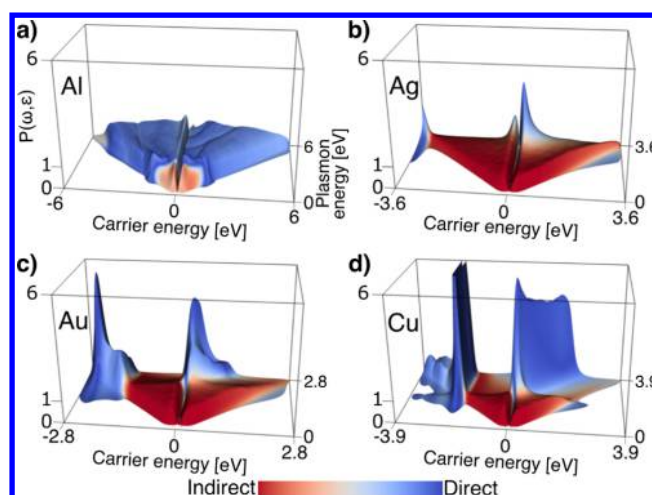

Figure 4. Energy distributions of hot carriers, $P(\omega,\varepsilon)$, generated by the decay of surface plasmons due to phonon-assisted and direct transitions, as a function of plasmon frequency (ω) and carrier energy (ε) in (a) Al, (b) Ag, (c) Au, and (d) Cu. The color scale indicates the relative contributions of phonon-assisted (red) and direct (blue) transitions. For each frequency, $P(\omega,\varepsilon)$ is normalized such that it equals 1 for a flat distribution, similar to the red plateaus below threshold where phonon-assisted transitions dominate. These distributions are for carriers generated at semi-infinite surfaces: geometry changes the relative contributions of interband and intraband contributions, as shown in Figure 3, but does not affect the carrier energy distributions within each contribution.

probability because of the Lorentzian broadening due to carrier line widths in energy conservation (equivalently, a consequence of the uncertainty principle). This causes the small contributions from direct transitions below threshold seen for the noble metals in Figure 4. Such contributions are dominant for short-lived carriers (large broadening) at plasmon frequencies below regions of strong interband transitions, such as the top of the d bands in the noble metals. The higher density of states close to the top of the flatter d bands makes this effect stronger in copper.

Direct transitions, shown in blue, dominate at high energies and exhibit the strong material dependence we previously discussed in detail in ref 18. For copper and gold, direct transitions occur from the d bands to unoccupied states above the Fermi level, which results in holes that are much more energetic than electrons. Aluminum exhibits a relatively flat distribution of electrons and holes, while silver exhibits a bimodal distribution of hot electrons as well as holes from direct transitions in a very narrow frequency range close to the maximum plasmon frequency.

Phonon-assisted transitions, shown in red, exhibit a flat distribution of electrons and holes extending from zero to the plasmon energy for all the metals. In aluminum, direct transitions are also possible below the threshold at 1.6 eV and contribute ∼25% of the generated carriers. Geometry-assisted intraband transitions (in the surface or sphere cases) have a similar phase space to phonon-assisted transitions and also generate flat distributions of electron and hole energies. Resistive losses compete with phonon-assisted transitions but dissipate thermally and do not generate energetic hot carriers. Due to this competition, below threshold, ∼30−50% of the absorbed energy is dissipated without hot carrier generation. Therefore, plasmonic hot carrier applications could benefit

from the higher efficiency above threshold, where direct transitions dominate by far and result in high-energy carriers. However, the stronger damping due to interband transitions weakens plasmonic field enhancement; the trade-off between this effect and higher energy carriers should be considered when designing hot carrier devices, by combining our results with electromagnetic simulations. Additionally, we predict aluminum to be an excellent candidate for general hot carrier applications since it allows direct transitions at all energies and has the smallest fraction of resistive loss (despite its absolute resistivity being higher than other metals).

Carrier Transport. In experiments, hot carriers generated by plasmon decay must live long enough or travel far enough to be collected or detected. The time and length scales of such nonequilibrium carrier transport have been the subject of much recent debate.[3,5,34] Recent theoretical estimates for the energy-dependent lifetimes of hot carriers in metals[19] show that band structure effects can play an important role, especially for holes in the d bands of noble metals. However, those calculations are based on a less-accurate nonrelativistic band structure and available only for gold and silver. Here, we present the results of calculations for the lifetimes and mean free paths of hot carriers as a function of energy using our more accurate band structure methods in all four metals considered above, accounting for electron−phonon and electron−electron scattering.

For the electron−electron scattering contribution, we calculate the imaginary part of the quasiparticle self-energy given by[35]

$$\text{Im} \, \Sigma_{\mathbf{q}n}^{e-e} = \int_{BZ} \frac{d\mathbf{q}'}{(2\pi)^3} \sum_{n'} \sum_{GG'} \tilde{\rho}_{\mathbf{q}'n',\mathbf{q}n}(\mathbf{G}) \tilde{\rho}^*_{\mathbf{q}'n',\mathbf{q}n}(\mathbf{G}')$$

$$\times \frac{4\pi e^2}{|\mathbf{q}' - \mathbf{q} + \mathbf{G}|^2} \text{Im}[\epsilon_{GG'}^{-1}(\mathbf{q}' - \mathbf{q}, \varepsilon_{\mathbf{q}n} - \varepsilon_{\mathbf{q}'n'})] \quad (7)$$

where $\tilde{\rho}_{\mathbf{q}'n',\mathbf{q}n}(\mathbf{G})$ is the plane-wave expansion of the product density $\sum_\sigma u_{\mathbf{q}'n'}^{\sigma*}(\mathbf{r}) u_{\mathbf{q}n}^\sigma(\mathbf{r})$ of Bloch functions with reciprocal lattice vectors $\mathbf{G}$, and $\epsilon_{GG'}^{-1}(\mathbf{k},\omega)$ is the microscopic dielectric function in a plane-wave basis calculated within the random-phase approximation. See ref 35 for a detailed exposition including its connection to the Fermi golden rule for electron−electron scattering. Here, we calculate eq 7 in JDFTx[36] using an explicit frequency integral with 0.1 eV resolution for the dielectric function, retaining local field effects with a kinetic energy cutoff of 200 eV. The remaining computational details are identical to the plasmon decay calculations described in the Methods section.

We calculate the electron−phonon scattering contribution to the electron line width using the Fermi golden rule

$$\text{Im} \, \Sigma_{\mathbf{q}n}^{e-ph} = \pi \int_{BZ} \frac{\Omega d\mathbf{q}'}{(2\pi)^3} \sum_{n'\alpha\pm} \left(n_{\mathbf{q}'-\mathbf{q},\alpha} + \frac{1}{2} \mp \frac{1}{2} \right)$$

$$\times \delta(\varepsilon_{\mathbf{q}'n'} - \varepsilon_{\mathbf{q}n} \mp \hbar\omega_{\mathbf{q}'-\mathbf{q},\alpha}) |g_{\mathbf{q}'n',\mathbf{q}n}^{\mathbf{q}'-\mathbf{q},\alpha}|^2 \quad (8)$$

where the electronic states, phonon modes, and electron−phonon matrix elements are computed exactly as for the phonon-assisted decay (see Methods section). Additionally, we use a dense 48 × 48 × 48 grid to sufficiently resolve the $\mathbf{q}'$ integral with electron and phonon occupations at standard temperature, $T = 298$ K.

We then calculate the total carrier line width $\text{Im}\Sigma_{\mathbf{q}n} = \text{Im}\Sigma_{\mathbf{q}n}^{e-e} + \text{Im}\Sigma_{\mathbf{q}n}^{e-ph}$, the carrier lifetime $\tau_{\mathbf{q}n} = \hbar/(2\,\text{Im}\Sigma_{\mathbf{q}n})$, and mean

free path $\lambda_{\mathbf{q}n} = v_{\mathbf{q}n} \tau_{\mathbf{q}n}$, where $\mathbf{v}_{\mathbf{q}n} \equiv \frac{\partial \varepsilon_{\mathbf{q}n}}{\partial \mathbf{q}}$ is the group velocity of electronic state $\mathbf{q}n$. Figure 5 shows the resulting carrier lifetimes
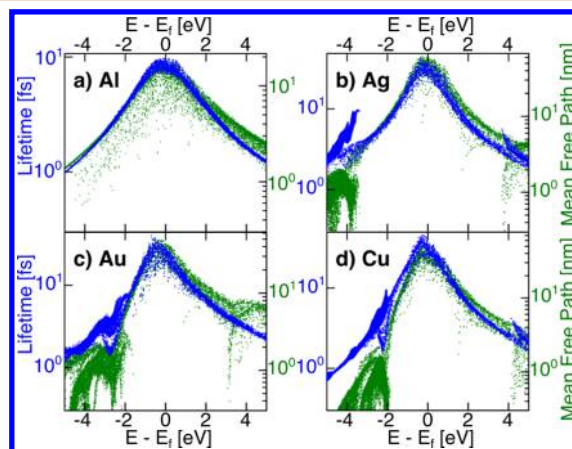

Figure 5. Hot carrier lifetimes as a function of energy, accounting for electron−electron and electron−phonon contributions for (a) Al, (b) Ag, (c) Au, and (d) Cu. For each panel, the left axis measures lifetime (blue) and the right axis measures mean free path (green). The spread in the results is because of multiple electronic states at each energy with different scattering rates due to anisotropy at the microscopic level (see Figure 6).

and mean free paths as a function of carrier energy relative to the Fermi level for aluminum and the noble metals. For each metal, the axes for lifetime and mean free paths have been scaled relatively by the Fermi velocity so that the two quantities coincide approximately for low energy carriers.

For all metals, we find that low-energy carriers close to the Fermi level have the longest lifetime and mean free path. At these energies, electron−phonon scattering dominates while electron−electron scattering, which is nominally proportional to $(\varepsilon - \varepsilon_f)^2$ due to the phase space available for scattering,[35] is negligible. The noble metals have similar maximum carrier lifetimes ~30 fs and mean free paths ~50 nm in the order Ag > Cu > Au, while aluminum has a smaller maximum lifetime ~10 fs and mean free path of ~20 nm. Our results for Au and Ag agree qualitatively with ref 19 but differ in the details for d band holes due to our refinement of the d band positions with the relativistic DFT+U method.[18]

With increasing carrier energy away from the Fermi level, for both electrons and holes, the electron−phonon scattering rates remain nominally constant while the electron−electron scattering rates increase dramatically, reducing the lifetimes and mean free paths. The electron−electron and electron−phonon contributions become comparable at roughly 1 eV away from the Fermi level for all four metals. The mean free paths drop to ~10 nm in all four metals for 2 eV electrons.

The spread in lifetimes at each energy is because states with different wave vectors at the same energy have different phase spaces and matrix elements for scattering due to the anisotropy of the material at the microscopic level. Figure 6 shows this anisotropy for carriers at the Fermi level for all four metals. Interestingly, the phase space for electron−phonon scattering increases in regions of positive Fermi surface curvature relative to those with negative curvature, causing a variation of about a factor of 2 in the lifetimes.

Figure 5 also exhibits an asymmetry between electron *versus* hole transport in all the metals. Electrons and holes of similar
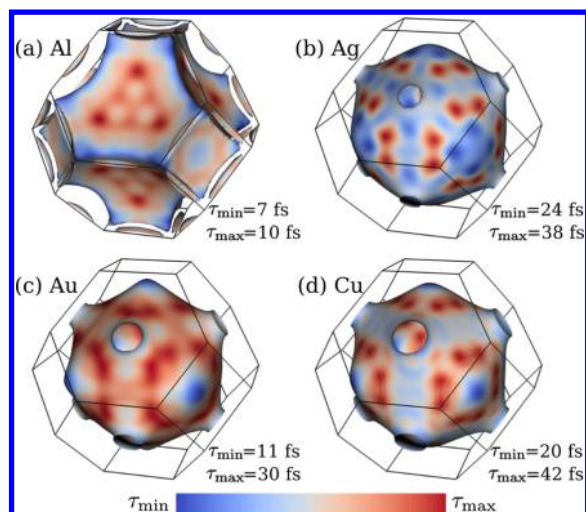
Figure 6. Anisotropy of hot carrier lifetimes on the Fermi surface of (a) Al, (b) Ag, (c) Au, and (d) Cu, with variations of about a factor of 2 between regions of positive and negative curvature of the Fermi surface.

energies have similar lifetimes, but electrons have higher group velocities and hence higher mean free paths because of the curvature of the dispersion relation. This effect is particularly drastic for d band holes in the noble metals, which are relatively localized states with dramatically smaller group velocities. However, after the first scattering event, d band holes result in s band holes with half the energy on average, which can transport much further. Additionally, our results indicate that aluminum and silver are particularly attractive for the transport of high-energy holes.

CONCLUSIONS

In this article, we report the first *ab initio* calculations of phonon-assisted optical excitations in metals, allowing us to link the energy range between resistive losses at low energies (microwave-infrared) and direct interband transitions at high energies (visible–ultraviolet). Along with surface-assisted transitions due to field confinement in metals,[16] this completes the theoretical picture of surface plasmon decay, accounting for all relevant mechanisms.

We find good agreement with experimental measurements for the total decay rate, but we additionally predict the relative contributions of all these processes and the initial generation of hot carriers in plasmonic metals. We find that direct transitions dominate above threshold and generate hot carriers, while below threshold, hot carrier generation by phonon-assisted transitions is diminished by competition from resistive losses. We also find that surface-assisted transitions are enhanced in nanoconfined geometries and become dominant below threshold for particle sizes ~10 nm, but that direct transitions remain dominant above the interband threshold even for small particles.

We suggest that aluminum is quite promising as a general purpose plasmonic hot carrier generator since it generates hot carriers efficiently for the widest frequency range and generates high-energy electrons and holes with equal probability. Compared to the noble metals, aluminum also exhibits the best transport properties for high-energy holes. A detailed analysis of the transport of energetic carriers in real metal nanostructures, based on the initial carrier distributions and

scattering rates predicted here, now enables directed design of optimal hot carrier devices.

METHODS

Electronic Structure. We require an approximation to quasiparticle energies and optical matrix elements to describe the decay of surface plasmons to quasiparticle excitations (eqs 2 and 3). We use the relativistic DFT+U approach that we previously established[18] to best reproduce experimental photoemission spectra in contrast to semilocal density functional or even quasiparticle self-consistent GW methods.[37] Strong screening in metals renders electron–hole interactions and excitonic effects negligible, so that we can work at the independent quasiparticle level rather than with the more expensive Bethe–Salpeter equation[38] that accounts for those effects.

Following ref 18, we perform density functional calculations in the open-source code JDFTx[36] with full-relativistic norm-conserving pseudopotentials at a plane-wave cutoff of 30 E_h (Hartrees). We use the PBEsol[39] exchange-correlation approximation and a rotationally invariant DFT+U correction[40] for the d electrons in noble metals (U = 1.63, 2.45, and 2.04 eV, respectively, for copper, silver, and gold). See ref 18 for more details regarding the selection of the electronic structure method.

We perform the self-consistent ground state calculations using a 12 × 12 × 12 uniform k-point mesh centered at the Γ point along with a Fermi–Dirac smearing of 0.01 E_h to resolve the Fermi surface. The optical matrix elements correspond to the momentum operator $\hat{p} \equiv \frac{m_e}{i\hbar}[\mathbf{r}, \hat{H}] = \frac{\hbar}{i}\nabla + \frac{m_e}{i\hbar}[\mathbf{r}, \hat{V}_{NL}]$, which accounts for the fact that the nonlocal DFT+U and pseudopotential contributions ($\hat{V}_{NL}$) to the DFT Hamiltonian ($\hat{H}$), do not commute with the position operator, $\mathbf{r}$. These nonlocal corrections are usually insignificant for s- and p-like electrons but are critical for describing optical transitions involving the d electrons in the noble metals.[33]

Finally, we interpolate the electronic energies and matrix elements to arbitrary k-points in the Brillouin zone using a basis of maximally localized Wannier functions.[41,42] Specifically, we use an sp^3 basis with four Wannier bands for aluminum and a relativistic d^{5}t^2 basis with 14 Wannier bands for the noble metals (where t is an orbital centered on the tetrahedral void sites of the face-centered cubic lattice). These Wannier functions exactly reproduce the orbital energies and matrix elements within the maximum surface plasmon energy of the Fermi level for all metals. We then evaluate eq 2 by Monte Carlo sampling 6.4 × 10^6 $\mathbf{q}$ values in the Brillouin zone for the noble metals (9.6 × 10^7 for aluminum) and histogram contributions by plasmon and carrier energies to get the direct transition results in Figures 2 and 4. Note that aluminum requires more $\mathbf{q}$ samples to get similar statistics since it contributes fewer pairs of bands per $\mathbf{q}$.

Phonon Modes and Matrix Elements. We calculate the *ab initio* force matrix for phonons and electron–phonon matrix elements from direct perturbations of atoms in a 4 × 4 × 4 supercell using exactly the same electronic DFT parameters as above in JDFTx.[36] All four metals considered here have a single atom basis and hence exactly three acoustic phonon modes. We then cast these phonon energies and matrix elements into a Wannier basis to enable interpolation for a dense sampling of the Brillouin zone integrals. (See ref 43 for a detailed introduction; we implement an analogous method in JDFTx, with additional support for spinorial relativistic calculations.)

We use the aforementioned Wannier basis to cover the energy range close to the Fermi level and add random-initialized maximally localized Wannier orbitals orthogonal to the first set to extend the energy range of included unoccupied states. We use a total of 24 Wannier bands for aluminum and 46 spinorial Wannier bands for the noble metals that exactly reproduce the orbital energies and optical and phonon matrix elements up to at least 50 eV above the Fermi level. We find this energy range of unoccupied states sufficient to fully converge the sum over states in the second-order perturbation theory (expression 3) at all plasmon energies considered.

Finally, we evaluate the double integral over Brillouin zone in eq 3 by Monte Carlo sampling with 2 × 10^7 {$\mathbf{q}$,$\mathbf{q}'$} pairs for the noble metals (3 × 10^8 pairs for aluminum to get similar statistics). We use

standard temperature, T = 298 K, to calculate the Fermi occupations for electrons and Bose occupations for phonons. Note that such low electronic temperatures (compared to the Fermi energy $\sim 10^5$ K) necessitate extremely dense Brillouin zone sampling, which is, in turn, made practical by the Wannier interpolation.[43] Histogramming by plasmon and carrier energies, we collect the phonon-assisted contributions to Figures 2 and 4 (after incorporating the extrapolation discussed below to eliminate sequential process contributions).

Extrapolation To Eliminate Sequential Processes. In the Results and Discussion section, we pointed out that eq 3 contains singular contributions when the intermediate state conserves energy (is "on-shell"), causing the denominators in the effective second-order matrix element to vanish. We examine these on-shell contributions in more detail here.

By taking the limit $\eta \to 0$ in eq 3 and noting that $|1/(x + i\eta)|^2 \to \pi\delta(x)/\eta$, we can show that

$$\lambda^* \cdot \mathrm{Im}\ \overline{\epsilon}_{\mathrm{phonon}}(\mathbf{q}'n', \mathbf{q}n) \cdot \lambda$$

$$= \frac{\mathrm{Im}\ \Sigma_{\mathbf{q}n'}^{\mathrm{e-ph}}}{\eta}(\lambda^* \cdot \mathrm{Im}\ \overline{\epsilon}_{\mathrm{direct}}(\mathbf{q}n', \mathbf{q}n) \cdot \lambda)$$

$$+ (\lambda^* \cdot \mathrm{Im}\ \overline{\epsilon}_{\mathrm{direct}}(\mathbf{q}'n', \mathbf{q}'n) \cdot \lambda)\frac{\mathrm{Im}\ \Sigma_{\mathbf{q}n}^{\mathrm{e-ph}}}{\eta}$$

$$+ O(\eta^0) + O(\eta^1) + \cdots \qquad (9)$$

where $\mathrm{Im}\ \overline{\epsilon}(\mathbf{q}'n',\mathbf{q}n)$ denotes the contribution to $\mathrm{Im}\ \overline{\epsilon}$ due to a specific pair of initial and final electronic states. Here, $\mathrm{Im}\Sigma^{\mathrm{e-ph}}{}_{\mathbf{q}n}$ is the electron line width due to electron–phonon scattering, given by eq 8.

The above expansion in η clearly illustrates that the singular contributions correspond to sequential processes. The first term corresponds to a direct transition followed by electron–phonon scattering, while the second term corresponds to the reverse. If we substitute the intermediate state line width $\mathrm{Im}\Sigma_{\mathbf{q}n}$ for η as the formalism prescribes,[20,21] and for simplicity focus only on electron–phonon scattering contributions $\mathrm{Im}\Sigma_{\mathbf{q}n}^{\mathrm{e-ph}}$ (which is dominant for low-energy carriers), then we see that the η singular part reduces simply to twice the direct contribution (eq 2). For a metal, this contribution should not be counted as a separate decay rate since scattering events preceding and following a transition are part of the initial Fermi distribution and the subsequent carrier transport, respectively.

We eliminate the singular contributions using an extrapolation scheme designed to exploit the fact that the η dependence is different for on-shell and off-shell processes. To retain the nonsingular $O(\eta^0)$ terms while canceling the $O(\eta^{-1})$ singular terms discussed above, we modify eq 3 as

$$(3)_{\mathrm{corrected}} = 2(3)|_{2\eta} - (3)|_{\eta} \qquad (10)$$

We find that η = 0.1 eV, which was previously used for semiconductors,[20] is sufficiently large to keep the singular terms resolvable for effective subtraction and sufficiently small to have negligible impact on the physical nonsingular contributions. We note that this extrapolation only has an effect and is necessary above the optical gap of the material. Previous *ab initio* studies of phonon-assisted processes[20,21] did not deal with this issue since they focused on predictions for semiconductors above the indirect gap and below the direct (optical) gap.

***Ab Initio* Estimate of Resistive Losses.** Single electron–hole pair generation dominates the plasmon decay at high frequencies. As the Results and Discussion section discusses, resistive loss in the metal, which arises from the finite carrier lifetime and results in heating rather than few energetic carriers, dominates at frequencies close to 0 eV. Here, we estimate these losses from the frequency-dependent resistivity calculated *ab initio* within a linearized Boltzmann equation with a relaxation time approximation.

The Boltzmann equation for electron occupations $f_{\mathbf{q}n}(t)$ in a uniform time-dependent electric field $\mathbf{E}(t)$ is[44]

$$\frac{\partial f_{\mathbf{q}n}(t)}{\partial t} + e\mathbf{E}(t) \cdot \frac{\partial f_{\mathbf{q}n}(t)}{\partial \mathbf{p}} = \frac{\partial f_{\mathbf{q}n}}{\partial t}\bigg|_{\mathrm{coll}} \qquad (11)$$

We then substitute $f_{\mathbf{q}n}(t) = f_{\mathbf{q}n} + \delta f_{\mathbf{q}n}(t)$, where the first term is the equilibrium Fermi distribution and the second contains perturbations to linear order due to the applied electric field, and collect contributions at first order in $\mathbf{E}(t)$.

To first order, the collision integral on the right-hand side of eq 11 can be written as $-\delta f_{\mathbf{q}n}\tau_{\mathbf{q}n}^{-1}$, where $\tau_{\mathbf{q}n}^{-1}$ is the difference between rates of scattering out of and into the electronic state $\mathbf{q}n$. Within the relaxation time approximation, we replace $\tau_{\mathbf{q}n}^{-1}$, which depends on the wave vector (Figure 6), by its average τ^{-1} (inverse of momentum relaxation time). This is an excellent approximation for metals where electron–phonon scattering dominates carrier relaxation near the Fermi level,[44] which is the case for most elemental metals (except those with partially occupied d shells) including aluminum and the noble metals.

Switching eq 11 to the frequency domain, linearizing, invoking the relaxation time approximation, and rearranging, we get

$$\delta f_{\mathbf{q}n}(\omega) = \frac{-ef'_{\mathbf{q}n}}{\tau^{-1} - i\omega}\mathbf{v}_{\mathbf{q}n} \cdot \mathbf{E}(\omega) \qquad (12)$$

where $\mathbf{v}_{\mathbf{q}n} \equiv \frac{\partial \varepsilon_{\mathbf{q}n}}{\partial \mathbf{q}}$ is the group velocity of electronic state $\mathbf{q}n$ and $f'_{\mathbf{q}n}$ is the energy derivative of the Fermi–Dirac distribution. We then calculate the current density $\mathbf{j} = \sum_{\mathbf{q}n} ef_{\mathbf{q}n}\mathbf{v}_{\mathbf{q}n}$ and obtain the conductivity tensor by factoring out $\mathbf{v}_{\mathbf{q}n}$. Averaging over directions, the isotropic conductivity is then

$$\sigma(\omega) = \frac{1}{1 - i\omega\tau}e^2\tau \underbrace{\int_{\mathrm{BZ}}\frac{d\mathbf{q}}{(2\pi)^3}\sum_n (-f'_{\mathbf{q}n})\frac{v_{\mathbf{q}n}^2}{3}}_{\equiv \sigma_0} \qquad (13)$$

where σ_0 is the zero-frequency (DC) conductivity.

Finally, we calculate the momentum relaxation time τ using the Fermi golden rule for electron–phonon scattering. In the average, we weight the scattering rates by $(-f'_{\mathbf{q}n})\frac{v_{\mathbf{q}n}^2}{3}$ since that determines the relative contributions to the conductivity above. It is then straightforward to show that $\tau^{-1} = \Gamma_{\mathrm{sum}}/w_{\mathrm{sum}}$, where

$$\Gamma_{\mathrm{sum}} = \frac{2\pi}{\hbar}\int_{\mathrm{BZ}}\frac{\Omega d\mathbf{q}d\mathbf{q}'}{(2\pi)^6}\sum_{n'n\alpha\pm}(-f'_{\mathbf{q}n})\frac{v_{\mathbf{q}n}^2 - \mathbf{v}_{\mathbf{q}n}\cdot\mathbf{v}_{\mathbf{q}'n'}}{3}$$

$$\times\left[n_{\mathbf{q}'-\mathbf{q},\alpha} + \frac{1}{2} \mp \left(\frac{1}{2} - f_{\mathbf{q}'n'}\right)\right]$$

$$\times\delta(\varepsilon_{\mathbf{q}'n'} - \varepsilon_{\mathbf{q}n} \mp \hbar\omega_{\mathbf{q}'-\mathbf{q},\alpha})\left|g_{\mathbf{q}'n',\mathbf{q}n}^{\mathbf{q}'-\mathbf{q},\alpha}\right|^2 \qquad (14)$$

with all the *ab initio* electron and phonon properties defined exactly as before and where the denominator for normalizing the weights is

$$w_{\mathrm{sum}} = \int_{\mathrm{BZ}}\frac{d\mathbf{q}}{(2\pi)^3}\sum_n (-f'_{\mathbf{q}n})\frac{v_{\mathbf{q}n}^2}{3} \qquad (15)$$

Note that with this definition, we can simplify the DC conductivity, $\sigma_0 = e^2\tau w_{\mathrm{sum}} = e^2 w_{\mathrm{sum}}^2/\Gamma_{\mathrm{sum}}$.

Given the frequency-dependent conductivity of the metal, we calculate the resistive losses as $\mathrm{Im}\ \epsilon = \mathrm{Im}[4\pi i\sigma(\omega)/\omega]$, which results in eq 6 upon simplification. We calculate w_{sum} and Γ_{sum} using Monte Carlo sampling of the Brillouin zone integrals with 1.6×10^6 $\mathbf{q}$ values for the single integral and 5×10^7 $\{\mathbf{q},\mathbf{q}'\}$ pairs for the double integral, which converges τ and σ_0 within 1%. Table 1 lists the momentum–relaxation time and resistivity we predict for the common plasmonic metals. The excellent agreement with experimental resistivities demonstrates the quantitative accuracy of the *ab initio* electron–phonon coupling (better than 10% in all cases).

Sensitivity Analysis. Finally, we test the robustness of our predictions against potential inaccuracies of the electronic structure

Table 1. *Ab Initio* Momentum Relaxation Times and Resistivities of Plasmonic Metals at $T = 298$ K, Compared to Experimental Resistivities from Reference 45

metal	τ (fs)	$\rho_0 = \sigma_0^{-1}$ (Ωm)	exptl ρ_0 (Ωm)
Al	11.5	2.79×10^{-8}	2.71×10^{-8}
Cu	35.6	1.58×10^{-8}	1.71×10^{-8}
Ag	36.4	1.58×10^{-8}	1.62×10^{-8}
Au	26.3	2.23×10^{-8}	2.26×10^{-8}

method, especially for phonon frequencies and electron−phonon couplings that can be highly sensitive to changes in lattice constants. Table 2 first shows that the PBEsol(+U) density functional method

Table 2. Relative Error in Predicted Equilibrium Lattice Constants (a) against Experimental Values[45] and Relative Change in the Resistivity, Scattering Time, Direct and Phonon-Assisted Contributions Measured When the Lattice Is Strained by 0.5%

metal	$\Delta a/a$	relative change with 0.5% strain			
		τ	ρ_0	Γ_{direct}	Γ_{phonon}
Al	−0.3%	15%	12%	6%	5%
Cu	+0.2%	9%	10%	3%	9%
Ag	+0.2%	1%	1%	5%	1%
Au	+0.5%	2%	5%	9%	3%

accurately predicts the lattice constants of all four metals to within 0.5% of experimental values, as expected based on its accuracy for metal geometries in general.[39]

We recalculate all our predictions after straining the lattice by 0.5% to conservatively estimate the uncertainty in those predictions due to DFT errors in structural annd phonon properties. Table 2 shows that the sensitivity is typically within 10%, in line with the agreement with experimental resistivities above. Somewhat counterintuitively, direct and phonon-assisted contributions are comparably sensitive to the lattice constant: the sensitivity of direct transitions arises from small changes in positions of electronic bands, whereas that of phonon-assisted transitions arises from the electron−phonon coupling. Additionally, the resistivity of aluminum is most sensitive because of a band crossing near the Fermi level, which shows up as the pockets near the Brillouin zone boundary in Figure 6 and strongly affects the density of states and electron−phonon lifetime near the Fermi level.

AUTHOR INFORMATION

Corresponding Authors
*E-mail: shankars@caltech.edu.
*E-mail: prineha@caltech.edu.
*E-mail: haa@caltech.edu.

Notes
The authors declare no competing financial interest.

REFERENCES

(1) Barnes, W. L.; Dereux, A.; Ebbesen, T. W. Surface Plasmon Subwavelength Optics. *Nature* **2003**, *424*, 824−830.

(2) Pendry, J. Playing Tricks with Light. *Science* **1999**, *285*, 1687−1688.

(3) Khurgin, J. B. How to Deal With the Loss in Plasmonics and Metamaterials. *Nat. Nanotechnol.* **2015**, *10*, 2−6.

(4) Maier, S. A. *Plasmonics: Fundamentals and Applications*; Springer Science and Business Media, 2007.

(5) Moskovits, M. The Case for Plasmon-derived Hot Carrier Devices. *Nat. Nanotechnol.* **2015**, *10*, 6−8.

(6) Mukherjee, S.; Libisch, F.; Large, N.; Neumann, O.; Brown, L. V.; Cheng, J.; Lassiter, J. B.; Carter, E. A.; Nordlander, P.; Halas, N. J. Hot Electrons Do the Impossible: Plasmon-Induced Dissociation of H2 on Au. *Nano Lett.* **2013**, *13*, 240−247.

(7) Robatjazi, H.; Bahauddin, S. M.; Doiron, C.; Thomann, I. Direct Plasmon-Driven Photoelectrocatalysis. *Nano Lett.* **2015**, *15*, 6155−6161.

(8) Clavero, C. Plasmon-Induced Hot-Electron Generation at Nanoparticle/Metal-Oxide Interfaces for Photovoltaic and Photocatalytic Devices. *Nat. Photonics* **2014**, *8*, 95−103.

(9) Christopher, P.; Xin, H.; Linic, S. Visible-Light-enhanced Catalytic Oxidation Reactions on Plasmonic Silver Nanostructures. *Nat. Chem.* **2011**, *3*, 467−472.

(10) Babicheva, V. E.; Zhukovsky, S. V.; Ikhsanov, R. S.; Protsenko, I. E.; Smetanin, I. V.; Uskov, A. Hot Electron Photoemission from Plasmonic Nanostructures: The Role of Surface Photoemission and Transition Absorption. *ACS Photonics* **2015**, *2*, 1039.

(11) Zheng, B. Y.; Zhao, H.; Manjavacas, A.; McClain, M.; Nordlander, P.; Halas, N. J. Distinguishing between Plasmon-induced and Photoexcited Carriers in a Device Geometry. *Nat. Commun.* **2015**, *6*, 7797.

(12) Leenheer, A. J.; Narang, P.; Lewis, N. S.; Atwater, H. A. Solar Energy Conversion via Hot Electron Internal Photoemission in Metallic Nanostructures: Efficiency Estimates. *J. Appl. Phys.* **2014**, *115*, 134301.

(13) Rakić, A. D.; Djurišić, A. B.; Elazar, J. M.; Majewski, M. L. Optical Properties of Metallic Films for Vertical-Cavity Optoelectronic Devices. *Appl. Opt.* **1998**, *37*, 5271−5283.

(14) Ordal, M. A.; Long, L. L.; Bell, R. J.; Bell, S. E.; Bell, R. R.; Alexander, R. W.; Ward, C. A. Optical Properties of the Metals Al, Co, Cu, Au, Fe, Pb, Ni, Pd, Pt, Ag, Ti, and W in the Infrared and Far Infrared. *Appl. Opt.* **1983**, *22*, 1099−1119.

(15) Etchegoin, P. G.; Le Ru, E. C.; Meyer, M. An Analytic Model for the Optical Properties of Gold. *J. Chem. Phys.* **2006**, *125*, 164705.

(16) Khurgin, J. preprint arXiv:1410.1226.

(17) Stanley, R. Plasmonics in the Mid-Infrared. *Nat. Photonics* **2012**, *6*, 409−411.

(18) Sundararaman, R.; Narang, P.; Jermyn, A. S.; Goddard, W. A.; Atwater, H. A. Theoretical Predictions for Hot-carrier Generation from Surface Plasmon Decay. *Nat. Commun.* **2014**, *5*, 5788.

(19) Bernardi, M.; Mustafa, J.; Neaton, J.; Louie, S. Theory and Computation of Hot Carriers Generated by Surface Plasmon Polaritons in Noble Metals. *Nat. Commun.* **2015**, *6*, 7044.

(20) Noffsinger, J.; Kioupakis, E.; Van de Walle, C. G.; Louie, S. G.; Cohen, M. L. Phonon-Assisted Optical Absorption in Silicon from First Principles. *Phys. Rev. Lett.* **2012**, *108*, 167402.

(21) Kioupakis, E.; Rinke, P.; Schleife, A.; Bechstedt, F.; Van de Walle, C. G. Free-carrier Absorption in Nitrides from First Principles. *Phys. Rev. B: Condens. Matter Mater. Phys.* **2010**, *81*, 241201.

(22) Hamaguchi, C. *Basic Semiconductor Physics*; Springer: Berlin, 2013.

(23) Tame, M. S.; Mcenery, K. R.; Özdemir, Ş. K.; Lee, J.; Maier, S. A.; Kim, M. S. Quantum Plasmonics. *Nat. Phys.* **2013**, *9*, 329.

(24) Archambault, A.; Marquier, F.; Greffet, J.-J.; Arnold, C. Quantum Theory of Spontaneous and Stimulated Emission of Surface Plasmons. *Phys. Rev. B: Condens. Matter Mater. Phys.* **2010**, *82*, 035411.

(25) Palik, E. D. *Handbook of Optical Constants of Solids*; Academic Press: New York, 1985.

(26) Sundararaman, R.; Narang, P.; Brown, A.; Atwater, H.; Goddard, W. A., III Surface-assisted decay dynamics in metal plasmonics, under review.

(27) Govorov, A. O.; Zhang, H.; Gun'ko, Y. K. Theory of Photoinjection of Hot Plasmonic Carriers from Metal Nanostructures into Semiconductors and Surface Molecules. *J. Phys. Chem. C* **2013**, *117*, 16616−16631.

(28) Manjavacas, A.; Liu, J. G.; Kulkarni, V.; Nordlander, P. Plasmon-Induced Hot Carriers in Metallic Nanoparticles. *ACS Nano* **2014**, *8*, 7630−7638.

(29) Zhang, H.; Govorov, A. O. Optical Generation of Hot Plasmonic Carriers in Metal Nanocrystals: The Effects of Shape and Field Enhancement. *J. Phys. Chem. C* **2014**, *118*, 7606−7614.

(30) Landau, L. On the Vibration of the Electronic Plasma. *J. Phys. (Moscow)* **1946**, *10*, 25−34.

(31) Bohm, D.; Pines, D. A Collective Description of Electron Interactions: III. Coulomb Interactions in a Degenerate Electron Gas. *Phys. Rev.* **1953**, *92*, 609−625.

(32) Elson, J. M.; Ritchie, R. H. Photon Interactions at a Rough Metal Surface. *Phys. Rev. B* **1971**, *4*, 4129−4138.

(33) Marini, A.; Onida, G.; Del Sole, R. Plane-Wave DFT-LDA Calculation of the Electronic Structure and Absorption Spectrum of Copper. *Phys. Rev. B: Condens. Matter Mater. Phys.* **2001**, *64*, 195125.

(34) Brongersma, M. L.; Halas, N. J.; Nordlander, P. Plasmon-Induced Hot Carrier Science and Technology. *Nat. Nanotechnol.* **2015**, *10*, 25−34.

(35) Ladstädter, F.; Hohenester, U.; Puschnig, P.; Ambrosch-Draxl, C. First-Principles Calculation of Hot-Electron Scattering in Metals. *Phys. Rev. B: Condens. Matter Mater. Phys.* **2004**, *70*, 235125.

(36) Sundararaman, R.; Gunceler, D.; Letchworth-Weaver, K.; Arias, T. A. *JDFTx*, http://jdftx.sourceforge.net, 2012; Accessed Oct 10, 2015 (revision# 1204).

(37) Rangel, T.; Kecik, D.; Trevisanutto, P. E.; Rignanese, G.-M.; Van Swygenhoven, H.; Olevano, V. Band Structure of Gold from Many-Body Perturbation Theory. *Phys. Rev. B: Condens. Matter Mater. Phys.* **2012**, *86*, 125125.

(38) Salpeter, E. E.; Bethe, H. A. A Relativistic Equation for Bound-State Problems. *Phys. Rev.* **1951**, *84*, 1232−1242.

(39) Perdew, J. P.; Ruzsinszky, A.; Csonka, G. I.; Vydrov, O. A.; Scuseria, G. E.; Constantin, L. A.; Zhou, X.; Burke, K. Restoring the Density-Gradient Expansion for Exchange in Solids and Surfaces. *Phys. Rev. Lett.* **2008**, *100*, 136406.

(40) Dudarev, S. L.; Botton, G. A.; Savrasov, S. Y.; Humphreys, C. J.; Sutton, A. P. Electron-Energy-Loss Spectra and the Structural Stability of Nickel Oxide: An LSDA+U Study. *Phys. Rev. B: Condens. Matter Mater. Phys.* **1998**, *57*, 1505−1509.

(41) Marzari, N.; Vanderbilt, D. Maximally Localized Generalized Wannier Functions for Composite Energy Bands. *Phys. Rev. B: Condens. Matter Mater. Phys.* **1997**, *56*, 12847−12865.

(42) Souza, I.; Marzari, N.; Vanderbilt, D. Maximally Localized Wannier Functions for Entangled Energy Bands. *Phys. Rev. B: Condens. Matter Mater. Phys.* **2001**, *65*, 035109.

(43) Giustino, F.; Cohen, M. L.; Louie, S. G. Electron-Phonon Interaction using Wannier Functions. *Phys. Rev. B: Condens. Matter Mater. Phys.* **2007**, *76*, 165108.

(44) Nozieres, P.; Pines, D. *Theory of Quantum Liquids*; Advanced Books Classics Series; Westview Press, 1999.

(45) Lide, D. *CRC Handbook of Chemistry and Physics*, 84th ed.; CRC Press, 2003.